Satellite-Based Clustering of Pre-Monsoon Wildfires and Variability of Tropospheric NO_2 and CO in Nepal

Dipson Bhandari[1]

[1] Independent Researcher, Nepal. Email: dipsonnec@gmail.com

[1] Corresponding author: Dipson Bhandari, Email: dipsonnec@gmail.com

Abstract

Nepal's pre-monsoon season transforms the country's southern lowlands into one of South Asia's most active wildfire landscapes. However, spatially explicit assessments of wildfire dynamics and trace gas variability at high temporal resolution remain limited. This study uses a satellite-based methodology to quantify wildfire activity and its atmospheric impacts across Nepal during 2021–2024. Visible Infrared Imaging Radiometer Suite (VIIRS) active fire observations were processed into a daily gridded dataset to derive fire count and fire radiative power (FRP) metrics. Wildfire hotspots and their spatial dynamics were identified using percentile-based thresholding combined with connected-component labeling to delineate contiguous clusters of extreme fire activity. Tropospheric nitrogen dioxide (NO_2) and total carbon monoxide (CO) were analyzed using Sentinel-5P TROPOMI products over these clusters across distinct physiographic zones from lowlands to Himalaya. Results reveal pronounced interannual variability in wildfire extent, with the largest hotspot cluster observed in 2022 (~6,718 km^2) across western and mid-western Nepal.

Fire activity exhibits a strong seasonal peak in April, accounting for 62% of annual detections. Wildfire episodes drive substantial trace gas enhancements, with NO_2 showing extreme intra-monthly variability including episodic increases exceeding 1,200% relative to baseline conditions. Lagged correlation analysis indicates peak associations between fire activity and trace gas concentrations at 1 day for NO_2 and 2 days for CO. Persistent hotspot regions are identified in the Terai and Siwalik zones, particularly in Bardiya, Banke, Dang, Surkhet, Parsa, and Bara districts. Despite limited local fire activity, enhanced seasonal and episodic trace gas patterns were also observed in the Himalayan region.

Keywords:

Wildfires, TROPOMI, VIIRS, Tropospheric NO_2, Carbon monoxide, Nepal, Fire clustering

1. Introduction

Forests cover a substantial portion of the Earth's land surface and play a critical role in regulating climate, biogeochemical cycles and ecosystems. In 2025, the global forest area was estimated at approximately 4.14 billion hectares, representing about 32% of the total land area worldwide (Global Forest Resources Assessment, 2025). However, forested regions across the globe are increasingly affected by wildfires. Between 2001 and 2020, the global annual burned area averaged approximately 774 million hectares, accounting for nearly 6% of all burnable land (Chen et al., 2023). The frequency, intensity, and spatial extent of wildfires have increased markedly in recent decades, driven primarily by climate change, land-use change, and prolonged dry conditions, even in regions that were previously less fire-prone (The State of the World's Forests, 2024).

Wildfires are a major source of atmospheric pollutants and significantly influence tropospheric chemistry. Emissions from wildland fires include greenhouse gases such as carbon dioxide (CO_2),

methane (CH_4), and nitrous oxide (N_2O), as well as photochemically reactive species including carbon monoxide (CO), non-methane volatile organic compounds (NMVOCs), and nitrogen oxides (NO_x). In addition, fires release substantial amounts of fine and coarse particulate matter (PM). Through both direct emissions and secondary chemical and physical processes, wildfires can severely degrade air quality and contribute to regional and long-range air pollution (Urbanski et al., 2008). Exposure to smoke from wildfire significantly increases the risk of premature mortality and cardiorespiratory morbidity in the general population, with particularly strong associations for cardiovascular deaths and asthma-related hospitalizations and emergency visits (Lei et al., 2024).

In South Asia, forest fires occur predominantly in India, Nepal, and Bhutan, collectively burning approximately 13,000–15,000 km² of forest annually, which represents about 1.7% of the region's total forest area (Aditi et al., 2025). Nepal is particularly vulnerable to seasonal wildfires due to its complex topography, diverse vegetation, and monsoon-dominated climate. Forest fires in Nepal are largely concentrated during the pre-monsoon season (March–May), when high temperatures, low relative humidity, and dry vegetation create favorable conditions for fire ignition and spread (Matin et al., 2017). Approximately 89% of all forest fires in Nepal occur during this period. (Bhujel et al., 2022). Long-term analyses indicate considerable interannual variability in forest fire occurrences and burned areas in Nepal between 2001 and 2020. On average, about 3,098 fire incidents were recorded annually, resulting in the burning of approximately 172,041 ha of forest area per year. April accounted for nearly 65% of fire incidents, followed by March (17%) and May (13%). Spatially, the greatest forest damage was observed in the Terai (4.74 ha km^{-2}) and Siwalik (4.65 ha km^{-2}) regions, followed by the Mid-hills (2.09 ha km^{-2}) and the High Mountain and Himalayan regions (1.57 ha km^{-2}). During the same period, forest fires were estimated to emit

approximately 3.30 million tons of carbon annually (Bhujel et al., 2022). Forest fires have become a recurring hazard in Nepal, growing increasingly intense with each passing year and influenced by changes in monsoonal patterns, deforestation, land-use change, forest management practices, and the impacts of climate change, including reduced rainfall and drier winter conditions (ICIMOD, 2025).

After 2016, the highest number of forest fire incidents were recorded in 2021 between March and April, with more than 6,000 forest fires detected across Nepal. These fires have been linked to an exceptionally dry winter season in 2020/2021, during which the country received only 25.33% of the 30-year average precipitation (1981–2010) from December 2020 to February 2021 and studies conducted during this period within the Kathmandu Valley reported extreme $PM_{2.5}$ concentrations, reaching maximum values of 199 μg m^{-3} during the pre-fire period and escalating to 371 μg m^{-3} and 280 μg m^{-3} during the first and second major fire events, respectively(Khadgi et al., 2024). Despite the growing severity of wildfire impacts, air quality studies in Nepal remain limited, with most research focusing primarily on particulate matter and black carbon (Gyawali et al., 2025). A study on Statistical modelling identified vegetation type as a major driver, with deciduous broadleaf forests contributing substantially to burned areas in the Terai and Chure, and needle-leaf forests dominating fire-prone zones in the Middle and High Mountains (Joshi et al., 2025a). Although the relationship between forest fires and biodiversity loss in Nepal has received considerable research attention (Dahal et al., 2025), the changing spatial patterns and impacts on atmospheric variability remain comparatively understudied. Recent modeling efforts have further highlighted the role of wildfires in deteriorating air quality in Nepal. The WRF-Chem model was applied over Nepal to simulate wildfire-generated air pollutants and their transport (Shrestha et al., 2025).Model outputs were evaluated using Sentinel-5P TROPOMI observations for a series of

wildfire events between November 2020 and April 2021. Their results revealed substantial wildfire-induced increases in atmospheric pollutant concentrations, including a 120% increase in NO_2, followed by 48% for $PM_{2.5}$, 35% for PM_{10}, 32% for CO, 28% for SO_2, and 17.5% for NH_3. These contributions were quantified by comparing pollutant concentrations simulated with and without wildfire emissions in the WRF-Chem framework. Similar integrated observational studies were identified as essential for supporting data-driven decision-making, particularly for identifying wildfire hotspots and quantifying their trace gas variability. Although the studies on wildfire hotspot and regional trend has been carried out, it is mostly centered towards specific districts or province, trends or air pollution estimation over a certain peak episodes in major cities (Joshi et al., 2025a; Karki et al., 2025) .Systematic characterization of spatial wildfire footprints and quantification of tropospheric NO_2 and CO variability across multiple recent yeas remain largely unaddressed .

Building upon these advances, the present study utilizes VIIRS data and Sentinel-5P TROPOMI observations to identify wildfire footprints across Nepal and to investigate the spatiotemporal variability of NO_2 and CO over the hotspots during 2021–2024. Raw swath-level VIIRS observations were filtered and gridded to generate fire metrics for Nepal spanning 2021–2024. Percentile-based thresholding and connected component labeling are applied to identify the spatial footprints of persistent wildfire hotspot clusters, and daily TROPOMI observations are used to investigate the spatiotemporal column variability of tropospheric NO_2 and total CO over these hotspots during 2021–2024. The findings of this study are intended to serve a broad range of applications, including forest fire risk planning and management, evidence-based policy formulation at government and community levels, assessment of fire impacts on biodiversity-

sensitive landscapes and protected areas, and support for public health researchers estimating population exposure to wildfire smoke across Nepal's most fire-affected regions.

2. Methods

This study covers the entire country of Nepal, a landlocked nation in South Asia, bordered by China (Tibet) to the north and India to the south, east, and west. Nepal has an area of about 147,516 km² and lies between approximately 26°22′–30°27′ N latitude and 80°40′–88°12′ E longitude. The country has steep range in elevation, from around 60 m above sea level in the southern plains to 8,848 m at the peak of Mount Everest in the north. Nepal's diverse topography and can be classified into five physiographic north–south zones (Figure 1) extending from east to west: Terai (below 300 m), Siwalik (300–700 m), Hill (700–2,000 m), Lesser Himalaya (2,000–2,500 m), and Higher Himalaya (2,500–8,848 m).The Terai (plains) region is a flat lowland zone. The Siwalik region, also known as the Churia Range, has highly rugged terrain. The Hill region consists of mountainous terrain with valleys and mid-elevation forests. The Himalayan region lies at higher elevations and includes some of the world's highest mountains. The year is generally divided into spring or pre-monsoon (March–May), summer (June–August), autumn (September–November), and winter (December–January). The monsoon season lasts from June to September, bringing most of the annual rainfall. For data development and extraction, this study uses a spatial domain spanning 26.3°–30.5° N latitude and 80.0°–88.5° E longitude (Fig. 1), which includes Nepal and some portions of southern China and northern India. However, all analyses are confined to the geographical boundary of Nepal.

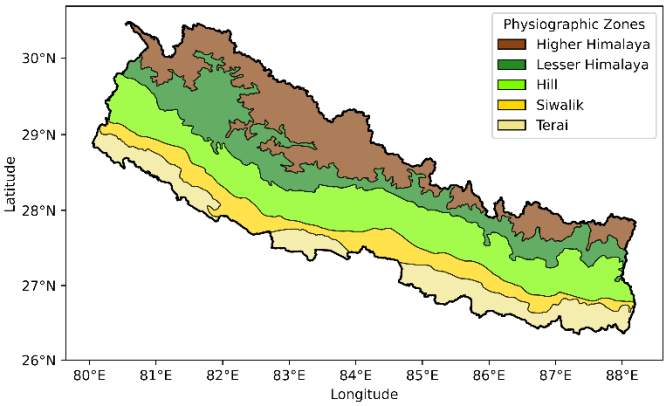

Fig. 1. Physiographic zones of Nepal.

2.1. Sentinel 5P TROPOMI Products from the Sentinel-5P Product Algorithm Laboratory (S5P-PAL)

TROPOMI is a nadir-viewing satellite sensor launched on October 13, 2017, aboard the Sentinel-5 Precursor satellite. It operates in a near-polar, sun-synchronous orbit at an altitude of 817 km, crossing the equator at approximately 13:30 local time in its ascending orbit and completing a full global coverage cycle every 17 days. With a high spatial resolution of up to 3.5 × 5.5 km², TROPOMI can detect localized pollution plumes and pinpointing small-scale emission sources and biomass burning events.

The Sentinel-5P Product Algorithm Laboratory (S5P-PAL), integrated into the Copernicus Dataspace Ecosystem in 2025, is a cloud-based platform for developing and testing Level 2 (L2) algorithms across the full Sentinel-5P data record (S5P-PAL, 2025). It offers distributed processing tools to advance algorithms to pre-operational stage. All pre-operational and operational L2 products are freely accessible through S5P-PAL data Portal. The platform also generates Level 3 gridded datasets at temporal averages ranging from daily to annual, produced using HARP, a data harmonization toolset for scientific Earth observation data (S&T Corporation, 2024). For this

study, Level 3 tropospheric NO_2 and CO products were utilized, which are available at a spatial resolution of 0.022° and 0.044° respectively across Nepal. Daily data of tropospheric NO_2 and total CO column density for the period 2021–2024 were obtained from the SP5-PAL data portal using Spatiotemporal Asset Catalog Application Programming Interface (STAC-API). The Copernicus Sentinel-5P level 3 data for NO2 and CO data are available pre-filtered for cloud contamination following the guidelines of the Product, with only measurements having a quality assurance value (qa_value) > 0.75 for tropospheric NO2 and qa_value > 0.5 for Total CO column. The data were extracted to the study domain shown in Figure 1, corresponding to 26.3°–30.5° N latitude and 80.0°–88.5° E longitude.

2.2. Processing and Gridding the VIIRS (VNP14IMG) Swath Product

The NASA Suomi-NPP Visible Infrared Imaging Radiometer Suite (VIIRS) Active Fire product provides high-resolution observations of global fire activity at ~375 m spatial resolution and ~12-hour temporal intervals. For this study, the Level 2 VIIRS 6-Minute Swath 375 m product (VNP14IMG) was utilized, which uses all five I-channels (I1–I5) and the 750 m M13 channel, applying a multispectral contextual algorithm based on the MODIS heritage to detect sub-pixel fires and thermal anomalies using fixed and contextual tests for day and night observations. The product provides geolocated fire detections along with fire radiative power (FRP), Fire Detection confidence (FP_confidence), Fire pixel's latitude and longitude, day/night flag, and other fire metrics (NASA, 2018).

The VNP14IMG product has an 8-bit image classification product ("fire mask") consisting of a two-dimensional array with $[x, y]$ dimensions. The fire mask contains 10 classes (0–9), where class 8 represents nominal-confidence fire pixels and class 9 represents high-confidence fire pixels. Fire pixel locations are provided as Fire Pixel Latitude (FP_latitude) and Fire Pixel Longitude

(FP_longitude) in the original product. VIIRS also provides the Level 3 product VNP14A1, which offers a 1-km gridded daily composite of VNP14 fire pixels detected within each grid cell. However, because this product only reports the maximum Fire Radiative Power (FRP) per grid cell, and the present study deals with total FRP counts per grid cell, the Level 2 Swath product (VNP14IMG) was used to reproduce a daily gridded product with total FRP counts and other required parameters. Daily VIIRS active fire observations were obtained from the 375-m Level-2 Swath product (VNP14IMG) for the region of Nepal (latitude 26.3°–30.5° N; longitude 80.0°–88.5° E) for the years 2021-2024. All swath files were first grouped by date. Each swath was processed individually, and fire detections were filtered using fire mask values of 8 and 9 only, corresponding to nominal- and high-confidence fire pixels.

A binning approach was then used to grid the level 2 VIIRS data into a regular latitude-longitude grid at ~ 0.022° resolution. Since, the original dataset is not on a uniform geographic grid, this approach enables calculation of fire activity within each grid cell. For a given day, let $\mathcal{F} = \{(lat_k, lon_k, P_k, d_k)\}_{k=1}^{N}$ denote the set of all fire detectio ns, where $lat_k$and $lon_k$are the latitude and longitude of fire k, $P_k$is its fire radiative power (FRP), and $d_k$is the day/night flag (1 for day, 0 for night). The spatial domain is divided into a regular latitude–longitude grid with edges $\{lat_0, \dots, lat_{n_{\text{lat}}}\}$and $\{lon_0, \dots, lon_{n_{\text{lon}}}\}$. Each fire is assigned to a grid cell (i, j)such that $lat_i \leq lat_k < lat_{i+1}$and $lon_j \leq lon_k < lon_{j+1}$. For each grid cell, the total fire count is computed as the number of fires in that cell, $\text{fire\_count}_{i,j} = |\mathcal{F}_{i,j}|$, while the sum and maximum of FRP are given by $\text{frp_sum}_{i,j} = \sum_{k \in \mathcal{F}_{i,j}} P_k$and $\text{frp\_max}_{i,j} = \max_{k \in \mathcal{F}_{i,j}} P_k$. The number of daytime and nighttime fires are calculated as $\text{day_count}_{i,j} = \sum_{k \in \mathcal{F}_{i,j}} \mathbf{1}_{\{d_k = 1\}}$and $\text{night\_count}_{i,j} = \sum_{k \in \mathcal{F}_{i,j}} \mathbf{1}_{\{d_k = 0\}}$, and the dominant detection time is the mode of the day/night flags within the cell,

196 $\text{day\_night\_mode}_{i,j} = \text{mode}\{d_k \mid k \in \mathcal{F}_{i,j}\}$. Grid cells with no detections are initialized to zero for
197 counts and sums and to undefined for FRP max and day/night mode. The gridded VIIRS variables
198 and Sentinel-5P tropospheric NO_2 and CO column densities were analyzed on a grid over Nepal.
199 Both datasets were processed for the period 2021–2024. Table 1 provides descriptions of the
200 variables calculated over grid cells, while (Fig. 2) shows example values of this dataset for the
201 period 1-7 April 2021 for NO_2, and additional illustration for CO is provided in Fig. S1.

202 **Table 1.** Names and descriptions of variables in the gridded VIIRS fire products over Nepal

Data Variables	Descriptions
Fire Count (Fire_count)	The total number of fire detections in each grid cell for the given day. Each fire detection is counted once per grid cell.
FRP sum (FRP_sum)	The sum of fire radiative power (FRP) of all fires within a grid cell. FRP is a measure of fire intensity in megawatts (MW).
FRP max (FRP_max)	The maximum fire radiative power detected in a grid cell. This identifies the single most intense fire in that cell
Day Count (Day_Count)	Number of fires detected during daytime in a grid cell
Night Count (Night_Count)	Number of fires detected during nighttime in a grid cell
Latitude Bounds (Lat_bnds)	The latitude edges of each grid cell

Longitude Bounds (Lon_Bnds)	The longitude edges of each grid cell

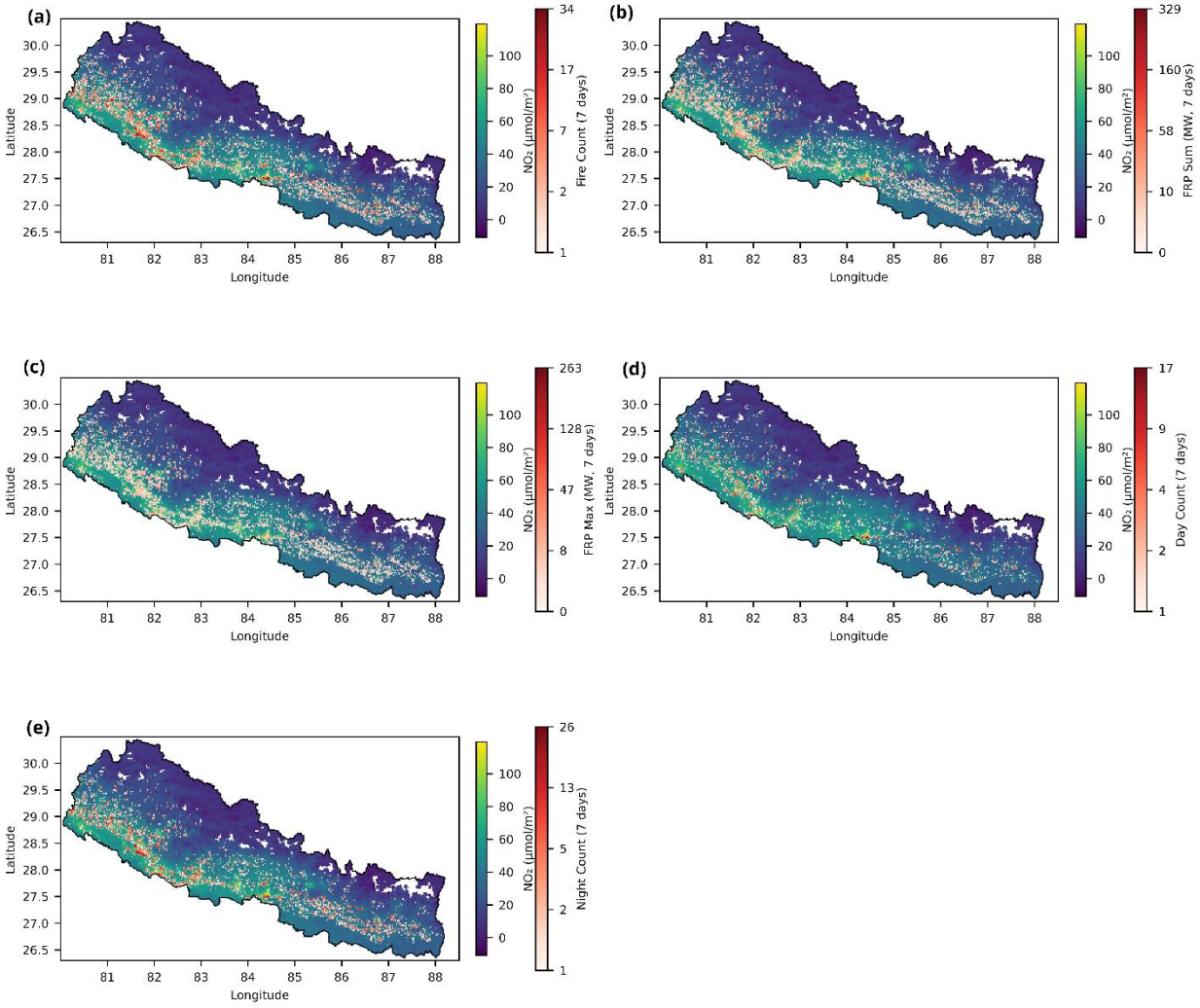

Fig. 2. Illustration of Seven-day mean (1–7 April 2021) tropospheric NO_2 column density (µmol/m²) from TROPOMI overlaid with VIIRS-derived fire variables across Nepal: (a) fire count, (b) FRP sum, (c) FRP max, (d) daytime fire count, and (e) nighttime fire count

2.3. Hotspot Algorithm

2.3.1. Hotspot Identification (Percentile-Based Thresholding)

Pre-Monsoon fire hotspot regions were identified using a combination of percentile-based thresholding and spatial connected component analysis applied to daily VIIRS gridded fire observations. Such files containing fire count and fire radiative power (FRP) were first aggregated over the full study time to produce pre-monsoon cumulative fire count and cumulative FRP fields for each grid cell.

For each grid cell within Nepal, hotspot was defined as a location where fire activity is specifically, 90th percentile thresholds of annual fire count or annual fire radiative power (FRP) across all cells in Nepal. A grid cell was marked as a hotspot if its annual fire count or FRP exceeded the corresponding 90th percentile threshold. Cells outside Nepal were not considered. Percentile-based thresholds allow identification of extreme fire activity relative to the regional background, avoiding the limitations of fixed absolute thresholds. fire count and FRP were combined to ensure that both frequently burning areas and regions with fewer but more intense fires are captured

2.3.2 Connected Component Labeling

Connected component labeling is one of the most important processes for image analysis, image understanding, pattern recognition, and computer vision (He et al., 2017). Connected component labelling is defined as a method where unique clusters in a image are identified based on connectivity to their sides or edges(Gonzalez & Woods, 2003). In 4-connected labeling, a pixel at coordinates (x, y) is considered connected only to the pixels that share an edge with it, namely the pixels at positions $(x \pm 1, y)$ and $(x, y \pm 1)$. In contrast, 8-connected labeling also considers diagonal neighbor pixels that share a corner, so connections can additionally occur with pixels at $(x \pm 1,$

y ± 1). Two-dimensional connected component labeling (CCL) is widely used in image analysis and has been applied to group fire pixels in images(Kantzas et al., 2015; Koltunov et al., 2012). Once hotspot pixels were identified pixel clustering was performed using a connected-component labeling (CCL) algorithm with 4-connected labelling. This method groups neighboring hotspot pixels into contiguous regions based on spatial adjacency, where pixels sharing a common edge (north, south, east, or west) are considered connected. Each connected group of hotspot pixels was assigned to a unique cluster identifier. The resulting hotspot clusters were ranked according to their spatial extent, quantified as the total number of largest interconnected grid cells within each cluster. Cluster size serves as a proxy for the areal extent of high fire activity. This study focuses on the top three largest contiguous clusters, which correspond to the areas or clusters of pixels where annual fire activity is extreme (top 10%). Each connected group of hotspot pixels was assigned with a unique integer cluster ID. For visualization purposes, cluster IDs are mapped to a discrete colormap (Fig. 3. Illustration of the top three wildfire clusters over Nepal in 2021.. The colors serve solely as visual separators to distinguish spatially distinct clusters and carry no physical meaning. Where the number of clusters exceeds the number of available colors, colors may repeat across non-adjacent clusters.

The cluster size $S_k$corresponds to the total number of grid cells belonging to that cluster. Only the hotspot cells themselves are counted; surrounding non-hotspot cells, cells from other clusters, or empty space inside the bounding box are not included (Fig. 4). For example, if 100 neighboring hotspot cells are connected, the cluster size is $S_k = 100$. The spatial extent of each cluster was described using a latitude–longitude bounding box defined by the minimum and maximum coordinates of the cluster cells. Clusters were ranked according to S_k, and the three largest clusters were selected for detailed spatial analysis and visualization. The area for affected region in the

cluster is calculated using equation (1) where A is the area of affected regions in the cluster. R is the radius of the earth, $(\lambda_2 - \lambda_1)$ is the longitudinal width of the region, φ_1 and φ_2 represents latitudes.

$$A = R^2 (\lambda_2 - \lambda_1) [sin(\varphi_2) - sin(\varphi_1)] \quad (1)$$

For analysis of column density variability, the entire boundary of each cluster was used to ensure that all regions potentially affected by the fires were included. This approach accounts not only for the main hotspot area but also for smaller internal clusters that may exist within a larger cluster, which could contribute to fire emissions and impact the surrounding region.

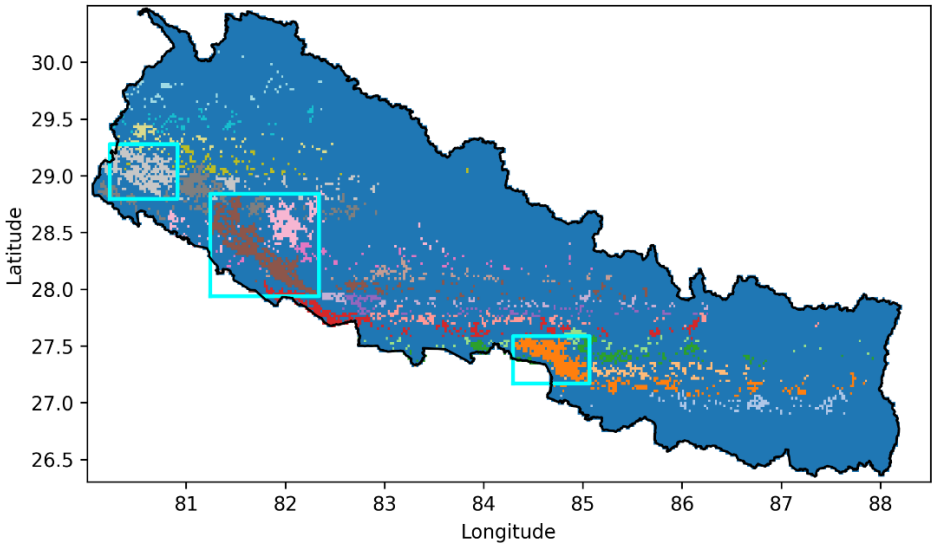

Fig. 3. Illustration of the top three wildfire clusters over Nepal in 2021.

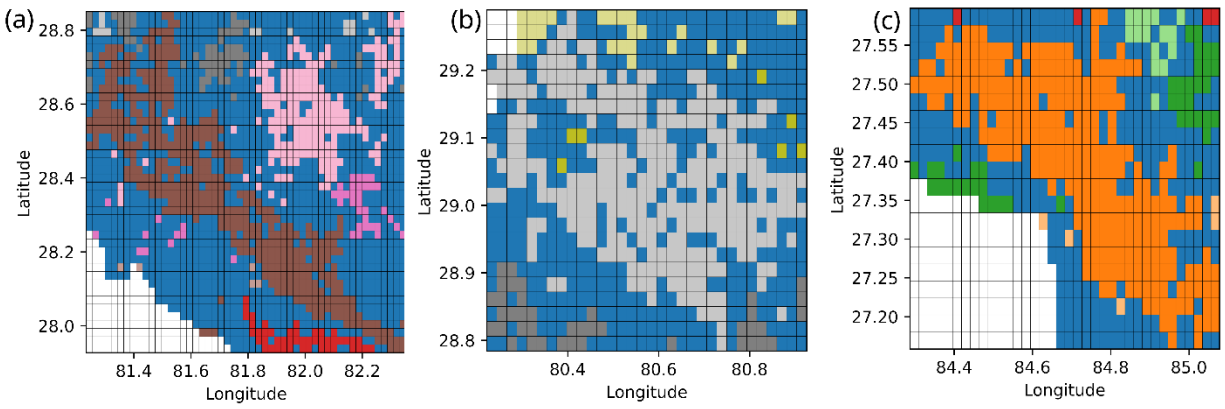

Fig. 4. Zoomed-in views of the top three fire clusters over Nepal in 2021 for pixel-level illustration. Panels (a), (b), and (c) correspond to the first, second, and third largest clusters.

2.4. Statistical Analysis of Trace Gas Variability

2.4.1. Seasonal Enhancement and Intra-Monthly Episodic amplitude

Daily cluster-averaged NO_2 and CO column densities were computed by spatially averaging all valid TROPOMI retrievals within each cluster bounding box. Monthly means and standard errors were computed from these daily values for each cluster, year, and month over the pre-monsoon period (March–May). Two metrics were used to characterize fire-driven trace gas variability. The first, seasonal enhancement (E_A), expresses the percentage increase of the monthly mean above the January–February pre-fire baseline for the same year and cluster:

Metric A: Seasonal Enhancement (%)

$$E_A = (\bar{X}_{month} - \bar{X}_{baseline})/\bar{X}_{baseline} \times 100 \quad (2)$$

where $\bar{X}_{\text{month}}$ is the monthly mean column density and $\bar{X}_{baseline}$ is the January–February baseline mean for the same cluster and year. January–February was selected as the background period because it precedes the fire season and exhibits minimal fire activity across all study years. The

second metric, intra-monthly episodic amplitude (E_B), captures the intensity of short-lived fire events within a month:

Metric B: Intra-monthly episodic amplitude (%)

$$E_B = (X_{max} - X_{min})/X_{min} \times 100 \quad (3)$$

where $X_{max}$and $X_{min}$are the maximum and minimum daily cluster-averaged column density within the month.

2.4.2. Monthly Spearman Correlation

To assess whether fire activity drives the observed trace gas enhancements, Spearman's rank correlation coefficient (ρ) was computed between the monthly total fire count and column densities across all cluster–year–month combinations. For each of the 3 clusters, 4 years (2021–2024), and 3 fire-season months (March–May), the total VIIRS-detected fire count within the cluster bounding box was aggregated, yielding a pooled dataset of up to 36 observations per correlation. Fewer than 3% of days were missing from the archive across all years and both trace gases, and these days were excluded from monthly mean calculations. Spearman's non-parametric rank correlation was selected as fire count distributions are strongly right-skewed (many low-fire months with occasional extreme events).

2.4.3. Lagged Daily Spearman Correlation

Since Metric B is computed once per month using only the monthly maximum and minimum values, a daily NO2 anomaly was used as a proxy for the episodic signal to check only the day-to-day fluctuation components.

$$X'(d) = X(d) - X_{Baseline}$$

where $X'(d)$ is the NO_2 anomaly on day d, $X(d)$ is the daily TROPOMI-measured column density, and $X_{Baseline}$ is the pre-fire-season baseline defined as the January–February mean for the corresponding cluster and year.

Despite its improved spatial resolution, TROPOMI's ability to capture short-lived atmospheric gases is constrained by its limited temporal resolution, particularly in mid-latitude regions where only one observation is typically available per day. This limitation can hinder accurate characterization of temporal variations in gas concentrations and introduce time-lag effects (Atalay et al., 2025). To investigate this effect, a lagged daily Spearman correlation was performed between daily fire counts and $X'(d + \text{lag})$ at lags of 0 to 3 days:

$$\rho_{lag} = Spearman(Fire(d),\ X'(d + lag))$$

where ρ_{lag} is the Spearman rank correlation coefficient at a given lag, $\text{Fire}(d)$ is the total VIIRS-detected fire count within the cluster on day d, $X'(d + \text{lag})$ is the NO_2 anomaly observed lag days after the fire, and lag is the temporal offset in days (0–3) representing the delay between fire and satellite-detected column enhancement.

3. Results and Discussion

3.1. Wildfire Trends

Over the period 2021–2024, fire activity in Nepal showed a pronounced seasonal cycle, with the highest occurrence between March and June, coinciding with the country's main dry season. The daily variation in VIIRS-detected fires from 2021 to 2024 (see Fig. 5) showed consistently low

fire activity during the winter and monsoon seasons, followed by a rapid increase during the pre-monsoon period. This seasonal peak can be driven by vegetation, topographic, and meteorological factors that create favorable conditions for forest fires(Joshi et al., 2025b). In 2021 (Fig. 5a), fire activity increased sharply from early March and peaked in April before declining with the onset of the monsoon. This period coincided with severe air-quality deterioration, prompting nationwide school closures when Kathmandu ranked among the most polluted cities globally. A similar but weaker seasonal pattern occurred in 2022 (Fig. 5b). In contrast, 2023 (Fig. 5c) exhibited a shorter yet more intense fire season, characterized by sharp peaks concentrated in April, while 2024 (Fig. 6d) showed sustained high fire activity throughout the pre-monsoon period, which indicates a longer and more severe fire season. Averaged over the four-year period, April alone accounted for approximately 62% of annual fire activity, consistently appearing as the peak month, with the highest contribution observed in 2022 (~70%). March and May contributed approximately 19% and 9%, respectively. These results show the dominant role of the pre-monsoon season in shaping fire activity across Nepal.

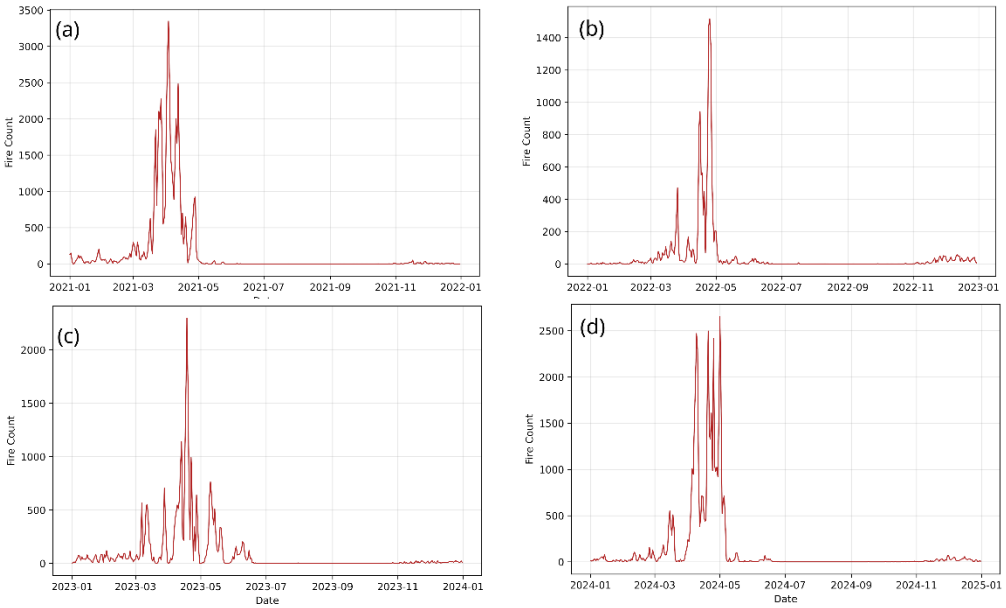

Fig. 5. Daily VIIRS fire counts over Nepal for the full year for (a) 2021, (b) 2022, (c) 2023, and (d) 2024.

3.2.Wildfire Hotspot and Affected Regions 2021-2024

Strong interannual and spatial variability in wildfire hotspots was observed across Nepal, with most fire activity concentrated in the western, mid-western, and central regions of the southern Terai belt (Fig. 6). In the southern plains, even slight slopes enhance drainage, leading to drier conditions and increasing the susceptibility of vegetation to fire, while prolonged precipitation deficits also contribute to extreme fire conditions in this region(Joshi et al., 2025b). In 2021, The largest cluster consisted of 425 connected hotspot grid cells, covering ~2,232 km², mainly in the mid-western districts of Bardiya, Banke, Dang, Surkhet, and Salyan. Smaller clusters were observed in the far-western districts (Dadeldhura, Doti, Kanchanpur, Kailali) and in the central–southern districts (Chitwan, Parsa, Bara), indicating localized wildfire hotspots (see Table 2). The year 2022 recorded the highest wildfire spatial extent. The largest cluster size of 1,279 connected grid cells fire and covered approximately 6,718 km², spreading across western and mid-western districts such as Kanchanpur, Kailali, Bardiya, Surkhet, Banke, Dang, and Arghakhanchi. This suggests widespread and intense wildfire conditions during that year. Smaller clusters were found in Dadeldhura and Baitadi, and in the southern plains (Parsa and Bara), which indicates that some areas remained repeatedly affected even during extreme years. In 2023, wildfire activity decreased compared to 2022 with cluster size of 377 over about 1,990 km², mainly in Dang, Arghakhanchi, Kapilbastu, Rupandehi, and Palpa. Another large cluster (375 connected hotspot grid; 1,972 km²) was concentrated in Bardiya, Banke, Dang, and Surkhet, while Chitwan, Parsa, and Bara continued to appear as persistent hotspots. In 2024, wildfire activity increased again but did not reach the 2022 level. The largest cluster had 598 fire events covering around 3,146 km², located mainly in

Bardiya, Banke, Dang, Surkhet, and Salyan. Overall, Bardiya, Banke, Dang, Surkhet, Parsa, and Bara appeared repeatedly as wildfire-prone districts across all four years (Fig. 6), indicating areas of consistent high risk. Substantial fire activity was also observed in northern India, particularly in regions adjacent to Nepal's southern border, which could influence atmospheric composition across the broader region. Indian cities and districts in these border areas, including Gorakhpur, Muzaffarnagar, and Varanasi in Uttar Pradesh, have been independently identified as wildfire hotspot zones during the pre-monsoon season (Majumdar, 2025).

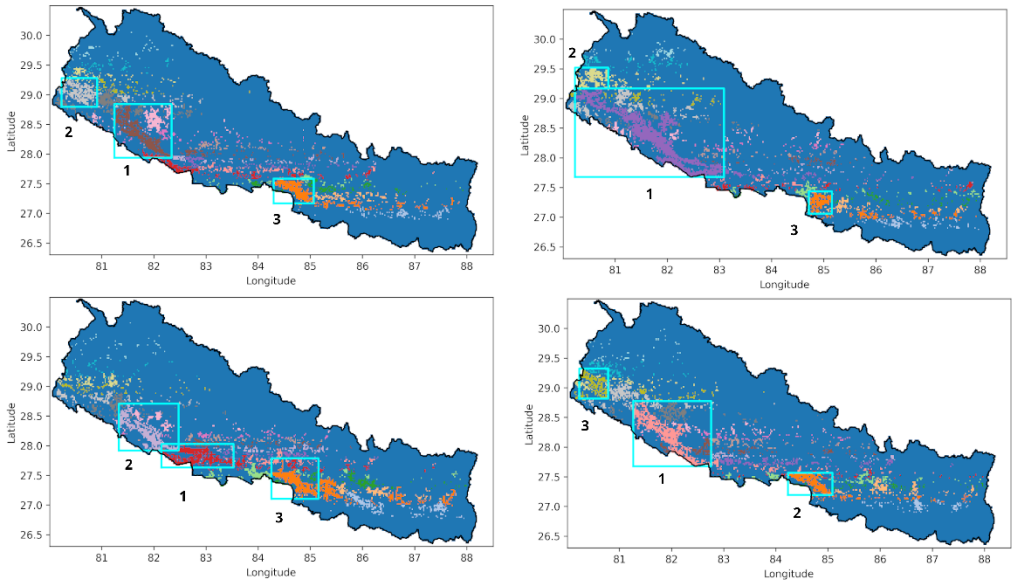

Fig. 6. Spatial extent of the three largest contiguous wildfire hotspot clusters across Nepal for each year from 2021 to 2024: (a) 2021, (b) 2022, (c) 2023, and (d) 2024.

Table 2. Cluster rank, number of connected hotspot grid cells, spatial extent (km²), and districts covered by each cluster.

Year	Rank	Cluster Size (Sk)	Area (km²)	Districts	Region
2021	1	425	2,232.20	Bardiya, Surkhet, Salyan, Banke, Dang	Mid-Western Terai
	2	260	1,356.85	Dadeldhura, Doti, Kanchanpur, Kailali	Far-Western Terai
	3	254	1,346.16	Chitwan, Parsa, Bara	Central Terai
2022	1	1,279	6,718.14	Kanchanpur, Kailali, Bardiya, Surkhet, Banke, Dang, Arghakhanchi	Far-Western to Mid-Western Terai
	2	202	1,051.17	Dadeldhura, Baitadi	Far-Western Hills
	3	166	880.85	Parsa, Bara	Central Terai
2023	1	377	1,990.47	Dang, Arghakhanchi, Kapilbastu, Rupandehi, Palpa	Mid-Western Terai–Hill Belt
	2	375	1,971.90	Bardiya, Banke, Dang, Surkhet	Mid-Western Terai
	3	295	1,563.41	Chitwan, Parsa, Bara	Central Terai
2024	1	598	3,145.65	Bardiya, Surkhet, Banke, Salyan, Dang	Mid-Western Terai

Year	Rank	Cluster Size (Sk)	Area (km²)	Districts	Region
	2	230	1,218.84	Chitwan, Parsa, Bara, Makwanpur	Central Terai
	3	189	986.15	Dadeldhura, Kailali, Doti	Far-Western Terai

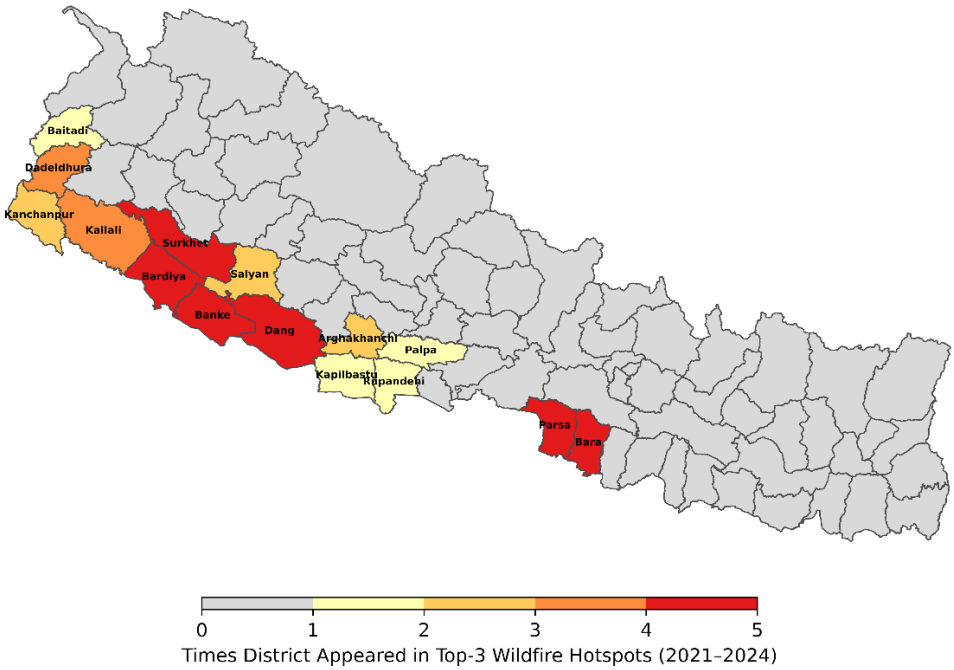

Fig. 7. District map of Nepal showing districts at risk based on the number of times they appeared in the Top 3 wildfire hotspot footprint during 2021–2024.

3.3. Tropospheric NO2 variability

Tropospheric NO_2 column densities over Nepal during 2021–2024 showed a strong and consistent pre-monsoon signal, with April consistently emerging as the peak month for seasonal enhancement across all clusters and years (see Fig. 8). Mean seasonal enhancements in April were 130% higher

than the January–February baseline during 2021–2024. This finding is consistent with, and slightly exceeds, the 120% wildfire-attributable NO_2 increase reported by Shrestha et al. (2025) for Nepal using WRF-Chem simulations. However, Shrestha et al.(2025) derived their estimate by comparing model simulations with and without fire emissions. The highest values was recorded in 2024, Cluster 2 which includes central-southern terai belt (Chitwan parsa and Bara) reached +177.6% (mean: 62.92 ± 3.81 μmol m^{-2}) with a single-day maximum of 124.46 μmol m^{-2} on April, the highest cluster-averaged daily value of the study period.

Intra-monthly episodic amplitudes were substantially larger, with the most extreme event recorded in April 2023 in Cluster 1 (~1,250%), where the daily maximum of 95.34 μmol m^{-2} in April exceeded the monthly minimum by approximately 13.5-fold, indicating an intense short-lived fire plume. This includes western Terai and adjoining hill districts (Kapilbastu, Rupandehi, Dang, Arghakhanchi, and Palpa. The western Terai corridor , particularly the Bardiya–Banke–Dang–Surkhet belt, appears as a persistent and dominant NO_2 hotspot, as the primary cluster in three out of four years. The central Terai (Chitwan–Parsa–Bara) consistently forms a secondary cluster and recorded the highest baseline NO_2 values among all clusters. This central Terai region contains extensive urban and industrial areas and has been identified as an NO_2 hotspot in previous studies, contributed by the high concentration of cement and brick factories (Gyawali et al., 2025) , which can drive its persistently elevated baseline values. The region also reached the highest monthly mean NO_2 column density of all clusters in April, with a value of 62.9 ± 3.8 μmol m^{-2}. The highest daily maximum NO_2 column density was recorded in April 2024, reaching 124.5 μmol m^{-2}

Spearman rank correlation between monthly VIIRS fire counts and Metric A (seasonal enhancement) yielded a strong and statistically significant association ($\rho = 0.820$, $p < 0.0001$), which indicates that the months with higher fire activity consistently corresponded to greater NO_2

enrichment above the pre-fire baseline across all clusters and years (see Fig.S2). A lagged daily Spearman analysis was conducted for lags of 0 to 3 days as mentioned in section 2.4.3. Daily fire counts were significantly correlated with same-day NO_2 at lag-0 (mean $\rho = 0.661$, $p < 0.0001$), with a marginal but consistent improvement at lag-1 (mean $\rho = 0.678$, $p < 0.0001$), followed by decline at lags 2 and 3 with $\rho = 0.658$ and 0.616, respectively (Fig.S2,Fig.S3).

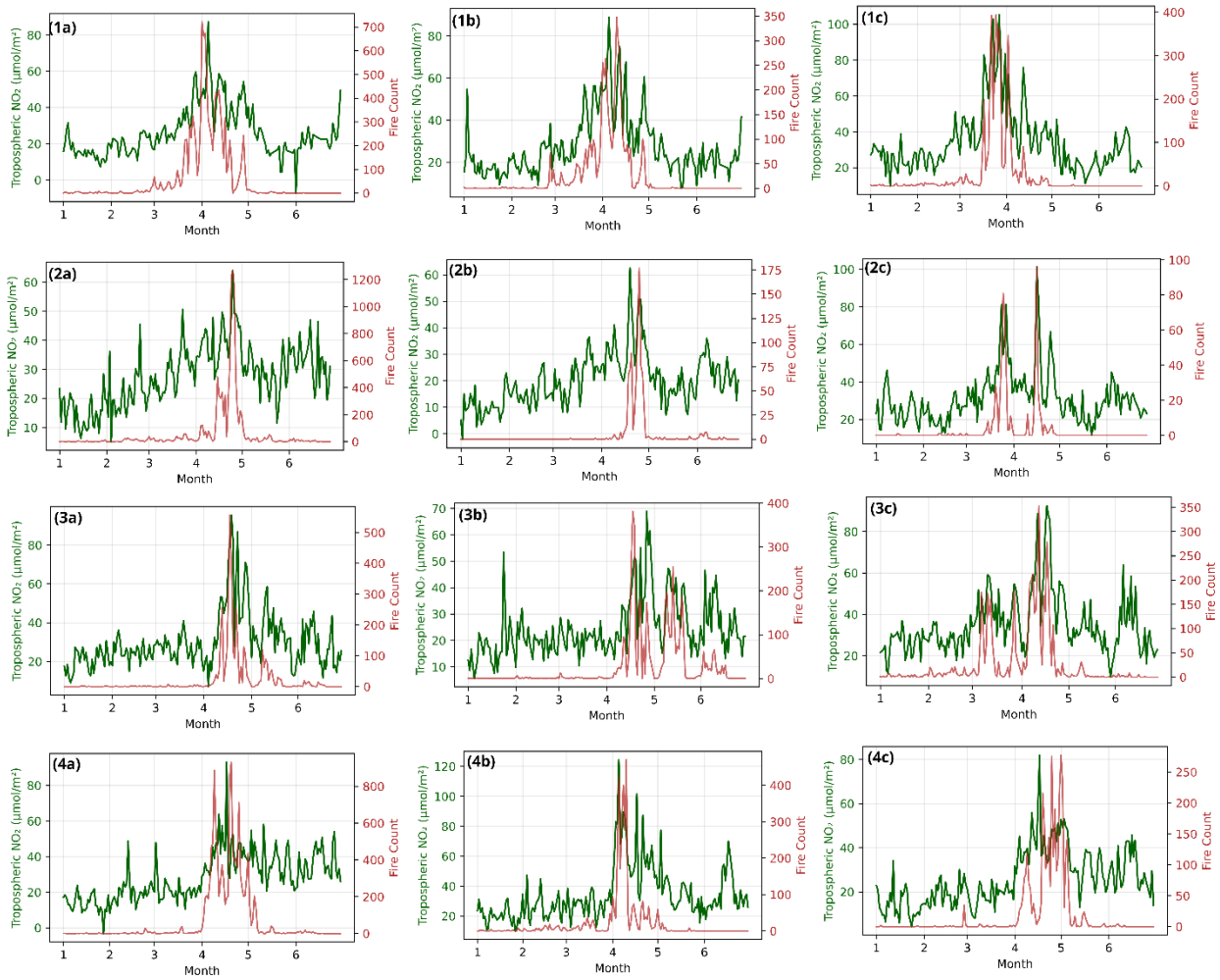

Fig. 8. Daily tropospheric NO_2 (µmol/m²) and fire counts for the three largest wildfire clusters in Nepal (January–June, 2021–2024). Panels show each year (rows 1–4) and cluster rank (columns a–c), where column 'a' is the largest cluster each year.

3.4. Total CO Column Variability over Hotspots

Total CO column concentrations over Nepal's Terai clusters during the pre-monsoon fire season (March–May, 2021–2024) showed consistent seasonal enhancement above the January–February baseline, with April dominating as the peak month across most clusters and years (Fig. 9). Cluster-averaged April enhancements reached approximately 39% in 2021, 35% in 2022, 19% in 2023, and 35% in 2024. The western Terai corridor (Bardiya–Surkhet–Banke–Salyan–Dang) consistently recorded the most intense episodic CO variability, with the most extreme event occurring in April 2021 when the daily maximum reached 109.4 mmol m^{-2} on April which is approximately 3.3 times the within-month minimum and showed an episodic amplitude of ~230% .This indicates a concentrated, high-intensity regional-scale fire episode. The central-southern Terai corridor (Chitwan–Parsa–Bara) consistently maintained the highest baseline CO concentrations across all years (up to 46.2 mmol m^{-2} in 2021) and repeatedly exhibited strong April episodic amplitudes peaking at ~189% in April 2021 and ~130% in April 2023. This can be attributed to the region's accumulative nature, compounded by the year-round anthropogenic emissions and high concentration of mines, brick kilns, and cement industries in this region (Gyawali et al., 2025; Joshi et al., 2025b). As this region is located near densely populated urban areas, targeted policy interventions and strengthened wildfire management during the pre-monsoon season are urgently needed.

Monthly Spearman correlation between VIIRS fire counts and CO seasonal enhancement (Metric A) was statistically significant (Fig.S4) but moderate ($\rho = 0.532$, $p < 0.001$), weaker than the corresponding NO_2 result ($\rho = 0.820$, $p < 0.0001$), and the lagged daily Spearman analysis (Fig.S5) indicated a progressive strengthening of the fire–CO relationship from lag-0 (mean $\rho = 0.457$, $p = 0.0163$) to a peak at lag-2 (mean $\rho = 0.566$, $p = 0.0001$), with consistently stronger correlations

observed at lag 1–2 days across all four individual years .CO seasonal enhancements were substantially more moderate than NO_2 across all clusters and years (CO Metric A range: ~15–53% vs NO_2 range: ~83–178%), and this weaker seasonal signal alongside the broader 2-day lag in contrast to the sharper 1-day peak observed for NO_2 (lag-1: $\rho = 0.678$, $p < 0.0001$). This is physically consistent with CO's longer atmospheric lifetime of several weeks, which maintains elevated background concentrations throughout the fire season, compresses the baseline-to-peak ratio, and allows fire-emitted CO to accumulate gradually in the tropospheric column over multiple days before reaching peak detectable concentrations at the TROPOMI overpass.

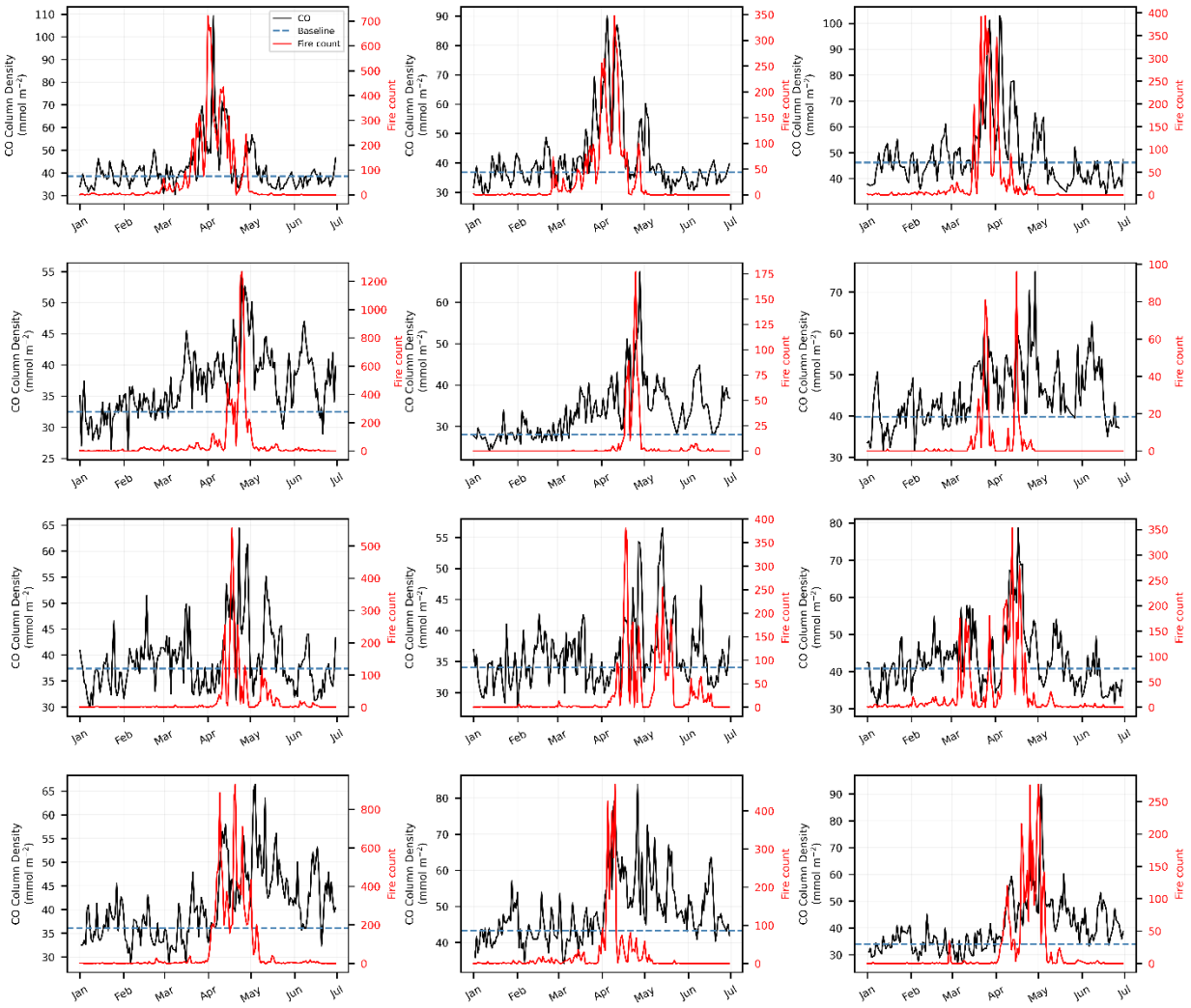

Fig. 9. Daily total column CO (mmol/m²) and fire counts for the three largest wildfire clusters in Nepal (January–June, 2021–2024). Panels show each year (rows 1–4) and cluster rank (columns a–c), where column 'a' is the largest cluster each year.

3.5. Trace Gas Variability in the Himalayan Region

Despite the Higher and Lesser Himalayan zones combined contributing approximately 7% of total VIIRS-detected fire activity during the pre-monsoon season, clear enhancements in both tropospheric NO_2 and total CO were observed during March–May across all four years (Fig. 10). Fire-season NO_2 enhancement over the Himalayan zone showed strong interannual variability, with the most extreme enhancements recorded in 2022 (March: +96.4%; April: +121.9%), coinciding with the anomalously large and spatially merged western Terai cluster spanning nearly 6,718 km² in that year (Fig. 11). Episodic NO_2 amplitudes over the Himalayan zone were large, with the most extreme events recorded in May 2024 (960.3%) and May 2022 (419.6%). These were months when the seasonal mean enhancement was near zero, which suggest that the individual fire plume transport events drive extreme single-day concentration spikes over the Himalayan zone rather than producing sustained baseline elevation. CO enhancements over the Himalayan zone were more moderate and temporally sustained than NO_2, with the highest values recorded in 2024 (April: +34.3%; May: +44.1%), making 2024 the most CO-impacted fire season over the Himalaya in the study period, while 2023 remained the least affected year across both gases. CO episodic amplitudes over the Himalayan zone (34–160%) were consistently and substantially lower than the corresponding NO_2 amplitudes (116–960%) and maintained elevated background concentrations in the Himalaya region.

The entire territory of Nepal lies within the Hindu Kush Himalaya region, a transboundary mountain system encompassing partial or complete territories of Afghanistan, Bangladesh, Bhutan, China, India, Myanmar, and Pakistan. Nepal's Himalayan zones are geographically proximate to the Indian and Bhutanese portions of this system, both of which are known to have high forest fire susceptibility (Ghale et al., 2026). Tracing the actual transport trajectories of these pollutants would require dedicated atmospheric transport modeling, which represents a potential avenue for future research to quantify the relative contributions of individual fire cluster events to trace gas enhancement in the Himalayan zone. In this study, a statistical approach is employed to provide a foundational understanding of this relationship. A pooled same-day Spearman rank correlation computed from the averaged NO_2 anomaly across all three Terai fire clusters and entire Himalayan zone NO_2 anomaly on the same day (Fig.S6), across all fire season days (March–May) of 2021–2024 combined , yielded $\rho = 0.585$ ($p < 0.0001$, $n = 361$). When computed separately for each year (Fig.S7), the correlation was significant in all four individual years: 2021 ($\rho = 0.788$), 2022 ($\rho = 0.740$), 2023 ($\rho = 0.401$), and 2024 ($\rho = 0.623$), which indicates that the linkage between the Terai lowlands and the Himalayan zone pre-monsoon enhancement is a consistent feature of Nepal. This finding is consistent with the preliminary assessment of transboundary transport of fire-induced air pollution ($PM_{2.5}$) from the lowland plains into the Himalayan region , which has been identified as an urgent regional air quality concern requiring integrated and transboundary approach to address air pollution episodes in Himalayan region (Mahapatra & Dhital, 2025).

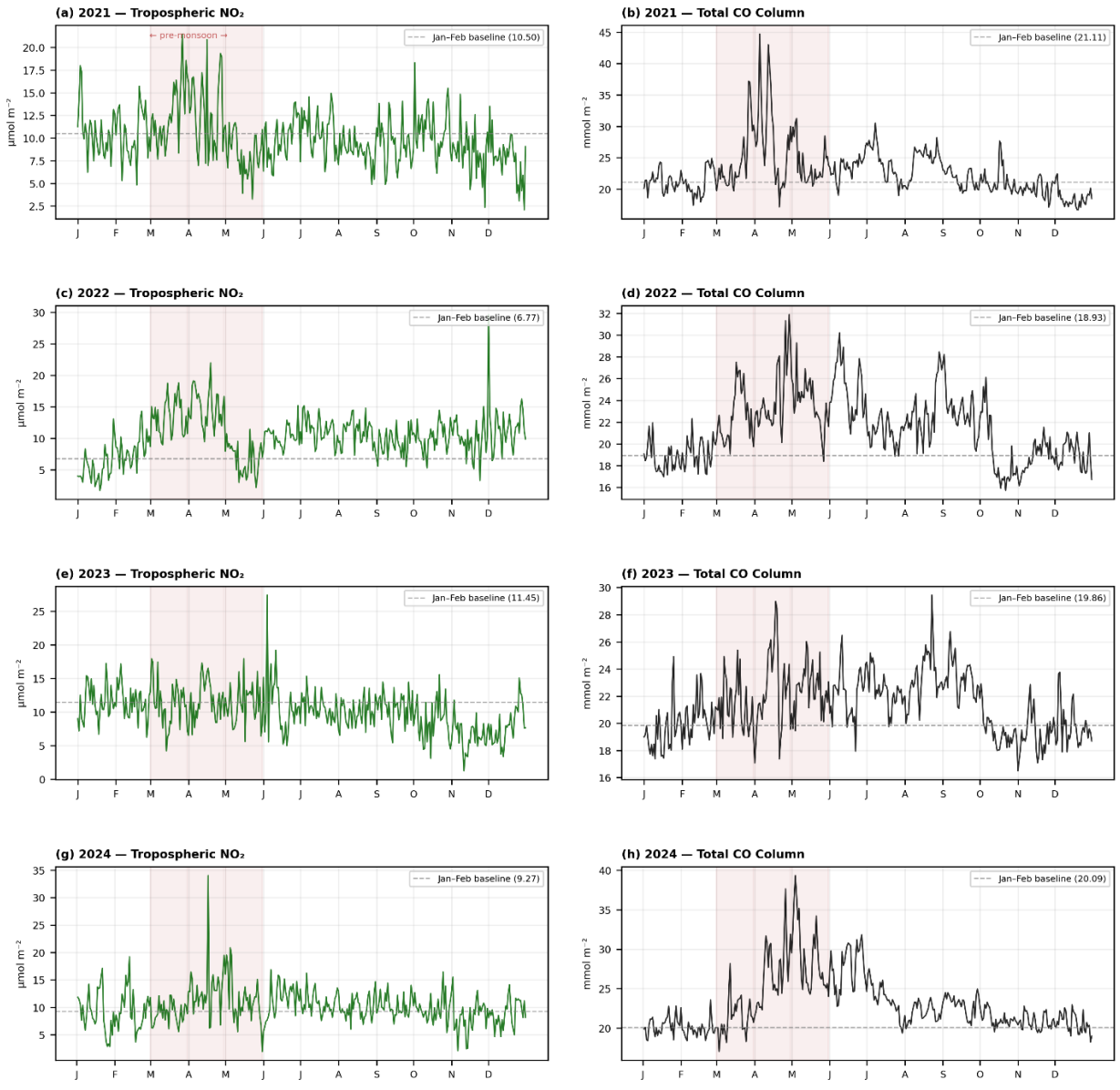

478

479 **Fig. 10.** Temporal variability of tropospheric NO_2 and CO column densities averaged over the

480 Lower and Higher Himalaya zones of Nepal.

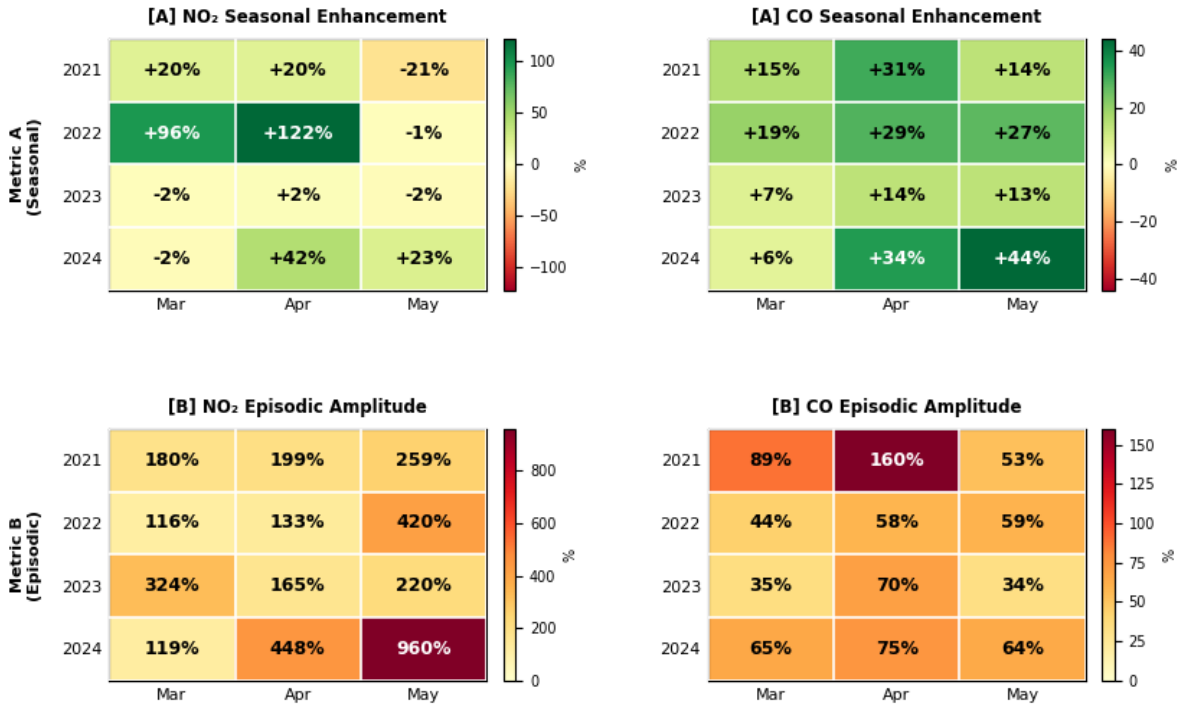

481

482 **Fig. 11.** Seasonal and Episodic Variability of Tropospheric NO_2 and CO over the Himalayan

483 Zone (2021–2024)

484 **4. Conclusion**

485 The study integrates VIIRS and Sentinel-5P TROPOMI observations to characterize the

486 spatiotemporal dynamics of pre-monsoon wildfires and their atmospheric impacts across Nepal

487 during 2021–2024. By combining percentile-based hotspot detection with connected-component

488 labeling and daily cluster-averaged trace gas analysis, the study provides a systematic and

489 quantitative assessment of wildfire footprints and associated NO_2 and CO variability at high

490 temporal resolution over Nepal.

491 Wildfire activity exhibited a consistent and pronounced seasonal cycle across all four years, with

492 April accounting for approximately 62% of annual fire detections. Strong interannual variability

was observed in both the spatial extent and intensity of wildfire hotspot clusters, with 2022 recording the largest contiguous cluster (~6,718 km²) spanning western and mid-western Nepal, while 2024 exhibited the most sustained fire season. Six districts -Bardiya, Banke, Dang, Surkhet, Parsa, and Bara appeared persistently in the top wildfire hotspot clusters across all four years, identifying these areas as regions of chronic and recurring fire risk that warrant prioritized management attention.

Tropospheric NO_2 showed the most dramatic fire-season response, with mean April seasonal enhancements of approximately 130% above the January–February pre-fire baseline, and intra-monthly episodic amplitudes reaching up to ~1,250% in April 2023. These extreme episodic spikes, driven by short-lived but intense fire plumes, highlight the acute air quality hazard posed by Nepal's pre-monsoon wildfires, particularly for populations in the Terai lowlands. Total CO column enhancements were more moderate (15–53% seasonal enhancement) and temporally broader, consistent with CO's longer atmospheric lifetime, which maintains elevated background concentrations throughout the fire season and produces a more gradual rather than episodic atmospheric loading. Lagged correlation analysis confirmed that NO_2 responds most strongly to fire activity at a 1-day lag, while CO peaks at a 2-day lag, findings that are physically consistent with the differing atmospheric lifetimes. A statistically significant same-day correlation was observed between lowland Terai fire cluster activity and trace gas anomalies over the Himalayan zone

Several limitations of this study should be acknowledged. The observed trace gas enhancements reflect contributions from all emission sources active during the fire season, including anthropogenic agricultural crop residue burning, urban and industrial activity, and transboundary pollution from northern India, and therefore cannot be fully attributed to forest fires alone without

dedicated atmospheric chemical transport modeling. Future research should employ models such as WRF-Chem or HYSPLIT to isolate fire-specific emission contributions and quantify long-term trends in transboundary pollutant transport across the Himalayan region during the pre-monsoon season. Additionally, further studies could also assess population exposure to air pollution in persistent wildfire hotspot districts and examine the situation of land-use change and forest management practices in these areas.

Given the recurring nature of pre-monsoon wildfires over recent decades, it is likely that this phenomenon will persist and potentially intensify under the influence of climate change. While the Government of Nepal, in collaboration with research institutions, established the Forest Fire Management System in 2021 to report fire incidents, governmental responses to wildfire dynamics and their atmospheric impacts remain limited and have received insufficient policy attention relative to their effects on biodiversity, atmospheric composition, and public health. Stronger coordination among government agencies, policymakers, and research institutions is therefore essential in a country like Nepal to formulate effective policies, strengthen enforcement mechanisms, and address the growing challenges of wildfire activity and deteriorating air quality.

Author contributions: CRediT

Dipson Bhandari: Conceptualization, Methodology, Software, Validation, Formal Analysis, Investigation, Data Curation, Writing-Original Draft, Writing-Review and Editing.

Funding

This research did not receive any specific grant from funding agencies in the public, commercial, or not-for-profit sectors.

Declaration of generative AI and AI-assisted technologies in the manuscript preparation process

During the preparation of this work the author used ChatGPT to assist with grammar correction, sentence restructuring, and language editing. After using this tool, the authors reviewed and edited the content as needed and take full responsibility for the content of the published article.

Data Availability

Data will be made available on request.

References:

Aditi, K., Pandey, A., & Banerjee, T. (2025). Forest fire emission estimates over South Asia using Suomi-NPP VIIRS-based thermal anomalies and emission inventory. *Environmental Pollution*, *366*, 125441. https://doi.org/10.1016/j.envpol.2024.125441

Atalay, H., Sunar, A. F., & Dervisoglu, A. (2025). Spatial Autocorrelation Analysis of CO and NO2 Related to Forest Fire Dynamics. *ISPRS International Journal of Geo-Information*, *14*(2), 65. https://doi.org/10.3390/ijgi14020065

Bhujel, K. B., Sapkota, R. P., & Khadka, U. R. (2022). Temporal and Spatial Distribution of Forest Fires and their Environmental and Socio-economic Implications in Nepal. *Journal of Forest and Livelihood*, *21*(1), 1–13. https://doi.org/10.3126/jfl.v21i1.56575

Chen, Y., Hall, J., Van Wees, D., Andela, N., Hantson, S., Giglio, L., Van Der Werf, G. R., Morton, D. C., & Randerson, J. T. (2023). Multi-decadal trends and variability in burned area from the fifth version of the Global Fire Emissions Database (GFED5). *Earth System Science Data*, *15*(11), 5227–5259. https://doi.org/10.5194/essd-15-5227-2023

Dahal, K., Talchabhadel, R., Pradhan, P., Parajuli, S., Shrestha, D., Chhetri, R., Gautam, A. P., Tamrakar, R., Gurung, S., & Kumar, S. (2025). Nepal's carbon stock and biodiversity are under threat from climate exacerbated forest fires. *Information Geography*, *1*(1), 100003. https://doi.org/10.1016/j.infgeo.2025.100003

Ghale, B., Mamgain, S., & Roy, A. (2026). Assessing Forest Fire Susceptibility in the Hindu Kush Himalaya: Implications for Biodiversity and Carbon Stock. *Journal of Geomatics*, *20*(1), 61–71. https://doi.org/10.58825/jog.2026.20.1.275

Global Forest Resources Assessment 2025. (2025). FAO. https://doi.org/10.4060/cd6709en

Gonzalez, R., & Woods, R. (2003). *Digital Image Processing Using MATLAB* (1st ed.).

Gyawali, M. S., Lamsal, L. N., Neupane, S., Gyawali, B., Bhattarai, K., Fisher, B., Krotkov, N., Van Geffen, J., Eskes, H., Sharma, S., Brunt, C., & Aryal, R. (2025). Cement and brick factories contribute elevated levels of NO2 pollution in Nepal: Evidence of high-resolution view from space. *Atmospheric Environment: X*, *26*, 100324. https://doi.org/10.1016/j.aeaoa.2025.100324

He, L., Ren, X., Gao, Q., Zhao, X., Yao, B., & Chao, Y. (2017). The connected-component labeling problem: A review of state-of-the-art algorithms. *Pattern Recognition*, *70*, 25–43. https://doi.org/10.1016/j.patcog.2017.04.018

ICIMOD. (2025). Forest Fires in Nepal: The Unseen Threat of Droughts. *Forest Fires in Nepal: The Unseen Threat of Droughts*. https://blog.icimod.org/cryosphere-water-risks/forest-fires-in-nepal-the-unseen-threat-of-droughts/

Joshi, K. P., Giri, S., Kuinkel, D., Kuikel, S., Devkota, R., Pradhananga, D., Marahatta, S., & Pokharel, B. (2025a). Forest fire dynamics in Nepal: Regional trends and socio-

ecological drivers. *Trees, Forests and People*, *21*, 100942. https://doi.org/10.1016/j.tfp.2025.100942

Joshi, K. P., Giri, S., Kuinkel, D., Kuikel, S., Devkota, R., Pradhananga, D., Marahatta, S., & Pokharel, B. (2025b). Forest fire dynamics in Nepal: Regional trends and socio-ecological drivers. *Trees, Forests and People*, *21*, 100942. https://doi.org/10.1016/j.tfp.2025.100942

Kantzas, E. P., Quegan, S., & Lomas, M. (2015). Improving the representation of fire disturbance in dynamic vegetation models by assimilating satellite data: A case study over the Arctic. *Geoscientific Model Development*, *8*(8), 2597–2609. https://doi.org/10.5194/gmd-8-2597-2015

Karki, G., Kunwar, R., Khadka, S., & Adhikari, S. (2025). Forest Fire Hotspots, Distribution and Management in Lowland of Tarai, Nepal. *Himalayan Biodiversity*, *10*, 70–83. https://doi.org/10.3126/hebids.v10i1.85810

Khadgi, J., Kafle, K., Thapa, G., Khaitu, S., Sarangi, C., Cohen, D., & Kafle, H. (2024). Concentration of particulate matter and atmospheric pollutants in the residential area of Kathmandu Valley: A case study of March–April 2021 forest fire events. *Environmental Pollution*, *363*, 125280. https://doi.org/10.1016/j.envpol.2024.125280

Koltunov, A., Ustin, S. L., & Prins, E. M. (2012). On timeliness and accuracy of wildfire detection by the GOES WF-ABBA algorithm over California during the 2006 fire season. *Remote Sensing of Environment*, *127*, 194–209. https://doi.org/10.1016/j.rse.2012.09.001

Lei, Y., Lei, T.-H., Lu, C., Zhang, X., & Wang, F. (2024). Wildfire Smoke: Health Effects, Mechanisms, and Mitigation. *Environmental Science & Technology*, *58*(48), 21097–21119. https://doi.org/10.1021/acs.est.4c06653

Mahapatra, P. S., & Dhital, N. B. (2025). Forest fire-induced air pollution events in the Himalayan region: Urgent need for regional collaboration and action. *BMC Environmental Science*, *2*(1), 13. https://doi.org/10.1186/s44329-025-00027-5

Majumdar, D. (2025). Decadal (2012–2023) account of spatio-temporal variability in satellite-detected biomass fires on Indian landmass and their fire radiative power. *Scientific Reports*, *15*(1), 27233. https://doi.org/10.1038/s41598-025-11200-w

Matin, M. A., Chitale, V. S., Murthy, M. S. R., Uddin, K., Bajracharya, B., & Pradhan, S. (2017). Understanding forest fire patterns and risk in Nepal using remote sensing, geographic information system and historical fire data. *International Journal of Wildland Fire*, *26*(4), 276–286. https://doi.org/10.1071/WF16056

NASA. (2018). *NASA VIIRS Land Science Investigator Processing System (SIPS) Visible Infrared Imaging Radiometer Suite (VIIRS) 375 m & 750 m Active Fire Products*. NASA. https://lpdaac.usgs.gov/documents/427/VNP14_User_Guide_V1.pdf

S5P-PAL. (2025). *Sentinel-5P Product Algorithm Laboratory*. Copernicus Dataspace Ecosystem. Copernicus Dataspace Ecosystem

Shrestha, K. L., Gyawali, A., Gyawali, S., Joshi, P., & Sharma, S. (2025). Modeling the impact of wildfire on air quality in Nepal using WRF-Chem and Sentinel-5P. *Environmental Pollution*, *382*, 126545. https://doi.org/10.1016/j.envpol.2025.126545

S&T Corporation. (2024). *HARP: Data harmonization toolset for scientific earth observation data* [Computer software].

The State of the World's Forests 2024. (2024). FAO. https://doi.org/10.4060/cd1211en

Urbanski, S. P., Hao, W. M., & Baker, S. (2008). Chapter 4 Chemical Composition of Wildland Fire Emissions. In *Developments in Environmental Science* (Vol. 8, pp. 79–107). Elsevier. https://doi.org/10.1016/S1474-8177(08)00004-1

Supplementary Information

Fig. S1. Illustration of Seven-day mean (1–7 April 2021) total CO column density (µmol/m²) from TROPOMI overlaid with VIIRS-derived fire variables across Nepal: (a) fire count, (b) FRP sum, (c) FRP max, (d) daytime fire count, and (e) nighttime fire count

Fig. S2. Spearman correlation between monthly fire count and seasonal NO_2 enhancement (left), and mean lagged daily correlation at 0–3 day lags (right).

Fig. S3. Spearman correlation between daily fire count and NO_2 column density at lags 0–2 days for each year (2021–2024) and cluster (C1–C3) during March–May.

Fig. S4. Spearman correlation between monthly fire count and seasonal CO enhancement (left), and mean lagged daily correlation at 0–3 day lags (right).

Fig. S5. Spearman correlation between daily fire count and CO column density at lags 0–2 days for each year (2021–2024) and cluster (C1–C3) during March–May.

Fig. S6. Same-day Spearman correlation between the averaged NO_2 anomaly across three Terai fire clusters and the Himalayan zone NO_2 anomaly during March–May 2021–2024 .

Fig. S7. Year-by-year Spearman correlation between averaged Terai and Himalayan zone NO_2 anomalies during March–May; all years significant ($p < 0.05$). Dashed line indicates the pooled correlation across all four years combined ($\rho = 0.585$).

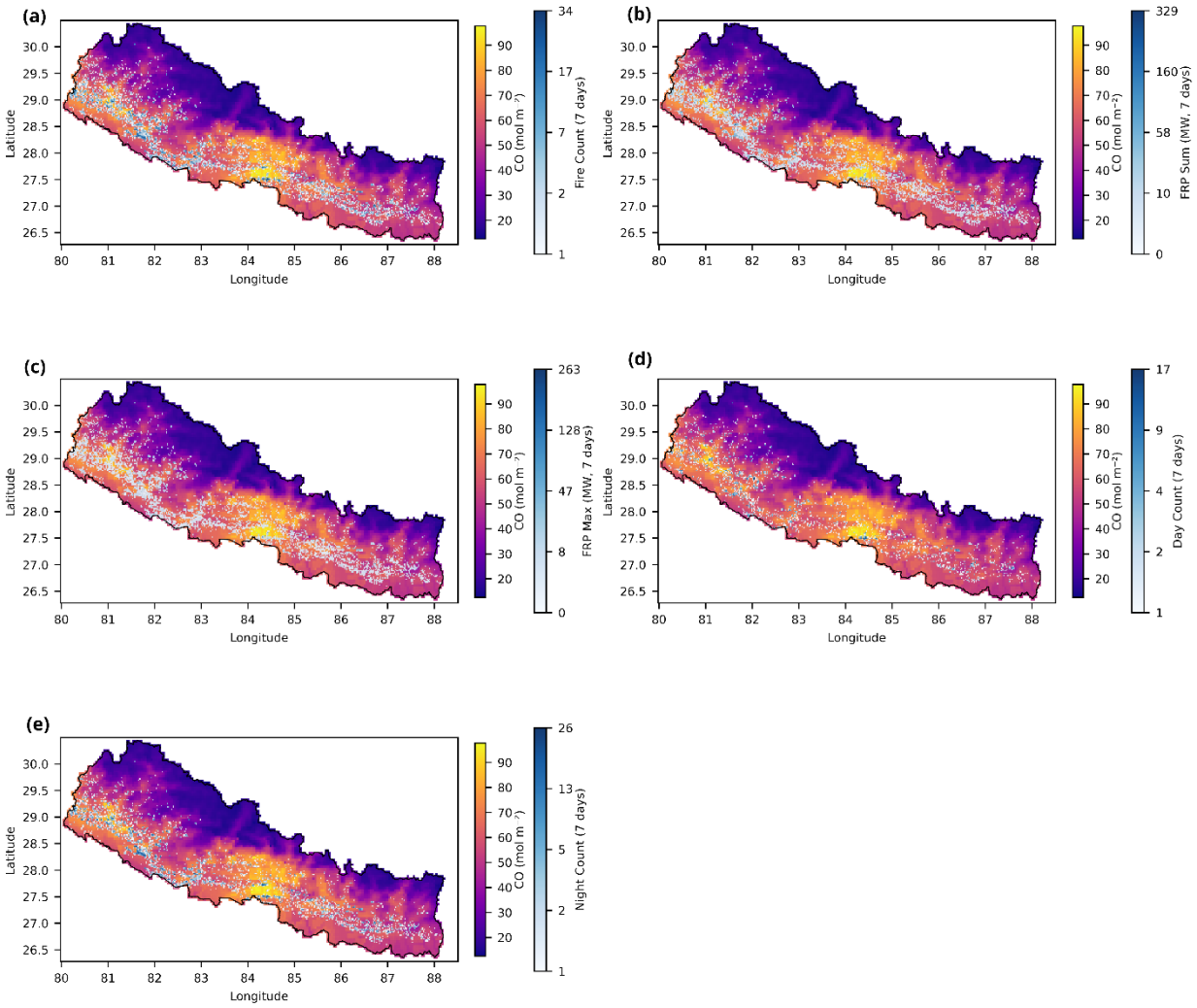

Fig. S1. Illustration of Seven-day mean (1–7 April 2021) total CO column density (µmol/m²) from TROPOMI overlaid with VIIRS-derived fire variables across Nepal: (a) fire count, (b) FRP sum, (c) FRP max, (d) daytime fire count, and (e) nighttime fire count

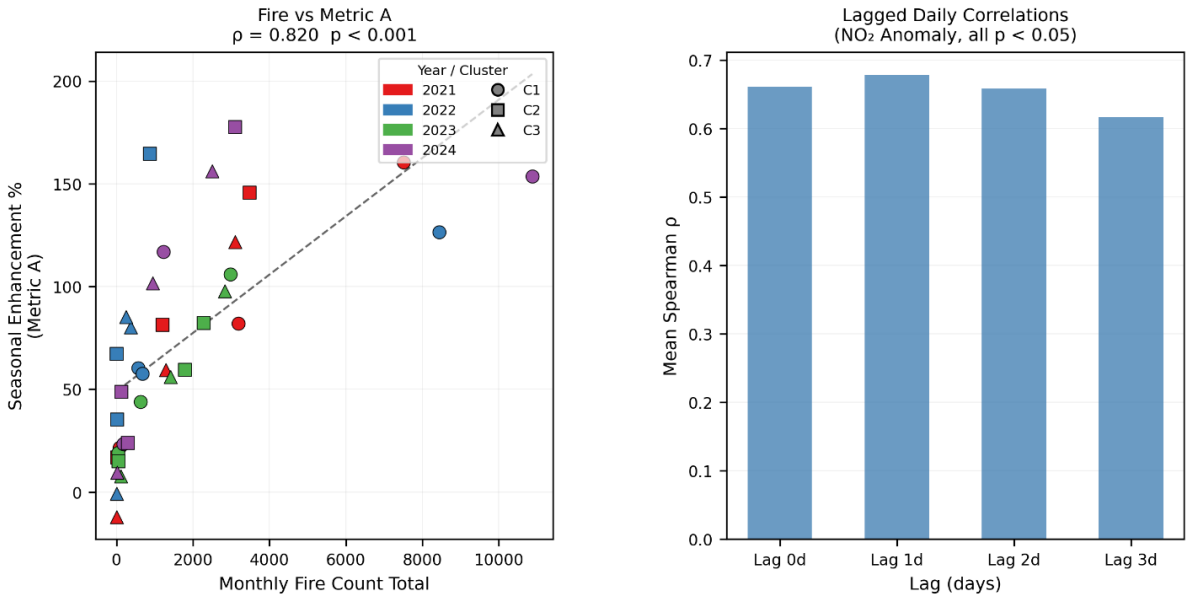

Fig. S2. Spearman correlation between monthly fire count and seasonal NO_2 enhancement (left), and mean lagged daily correlation at 0–3 day lags (right).

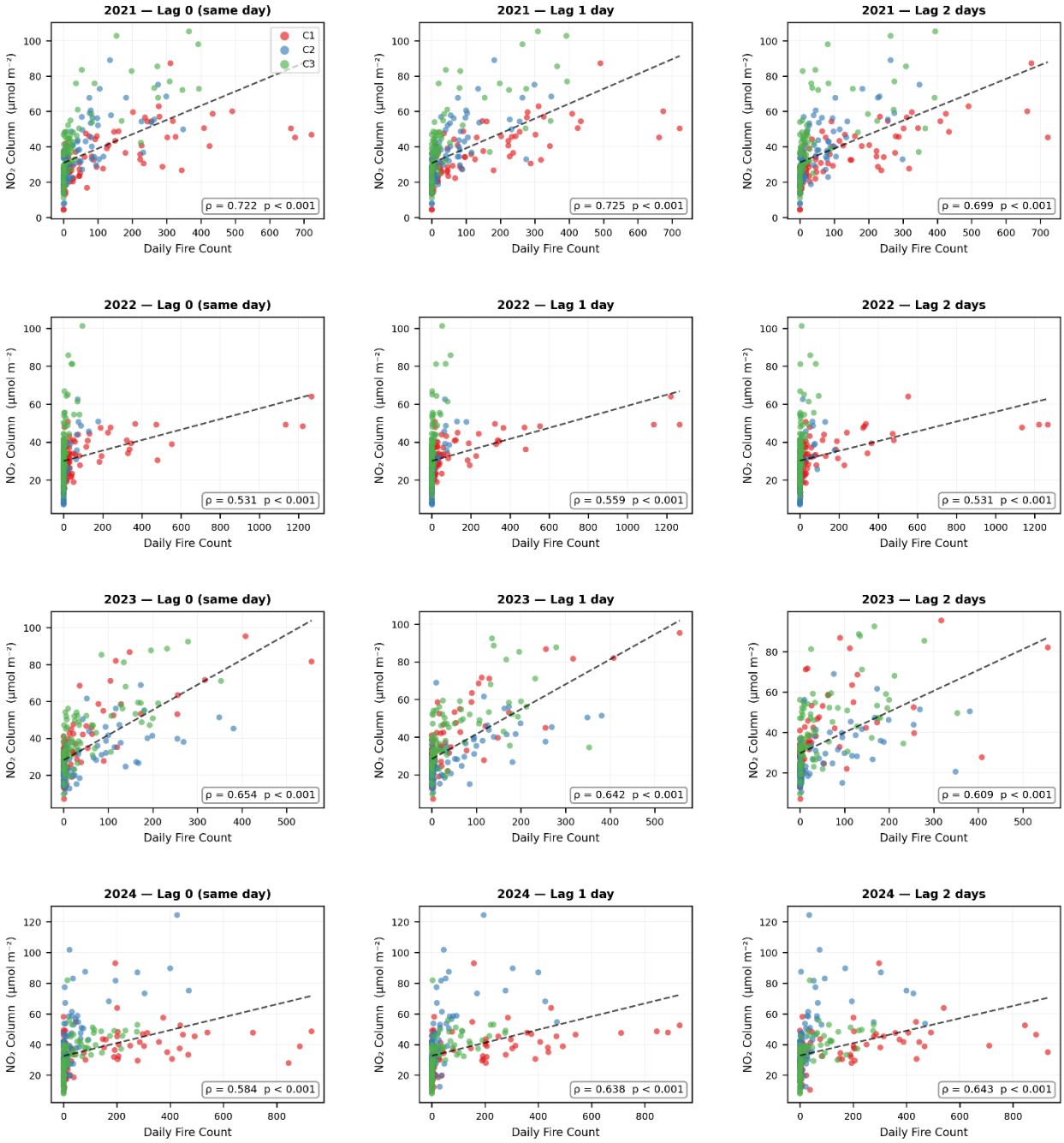

Fig. S3. Spearman correlation between daily fire count and NO_2 column density at lags 0–2 days for each year (2021–2024) and cluster (C1–C3) during March–May.

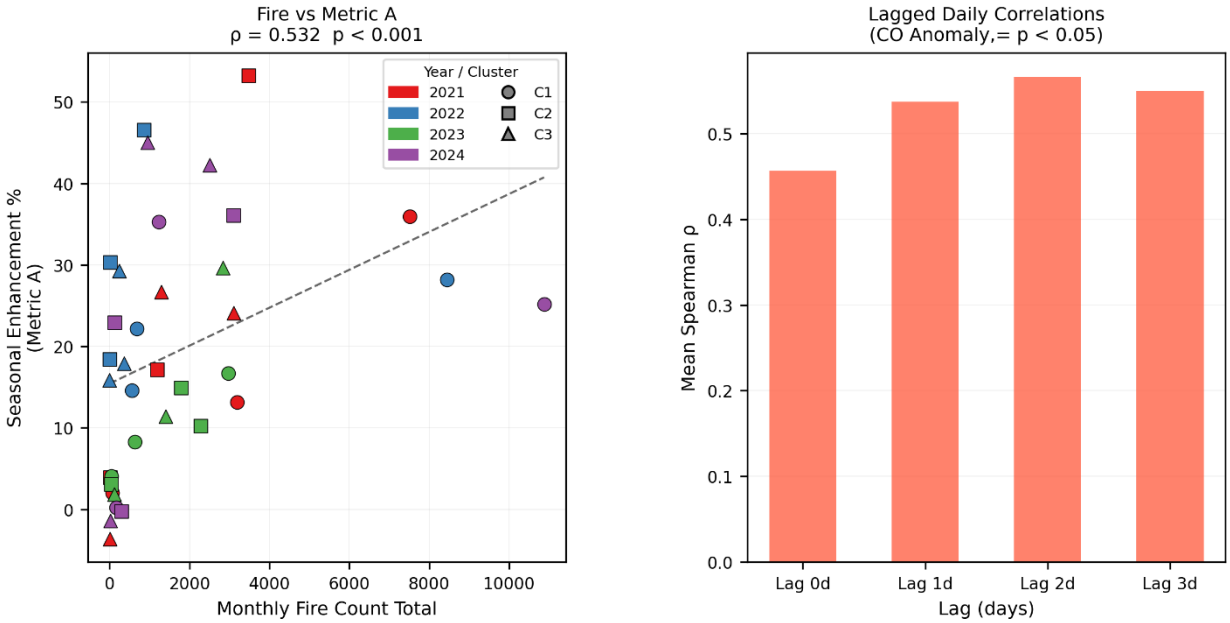

Fig. S4. Spearman correlation between monthly fire count and seasonal CO enhancement (left), and mean lagged daily correlation at 0–3 day lags (right).

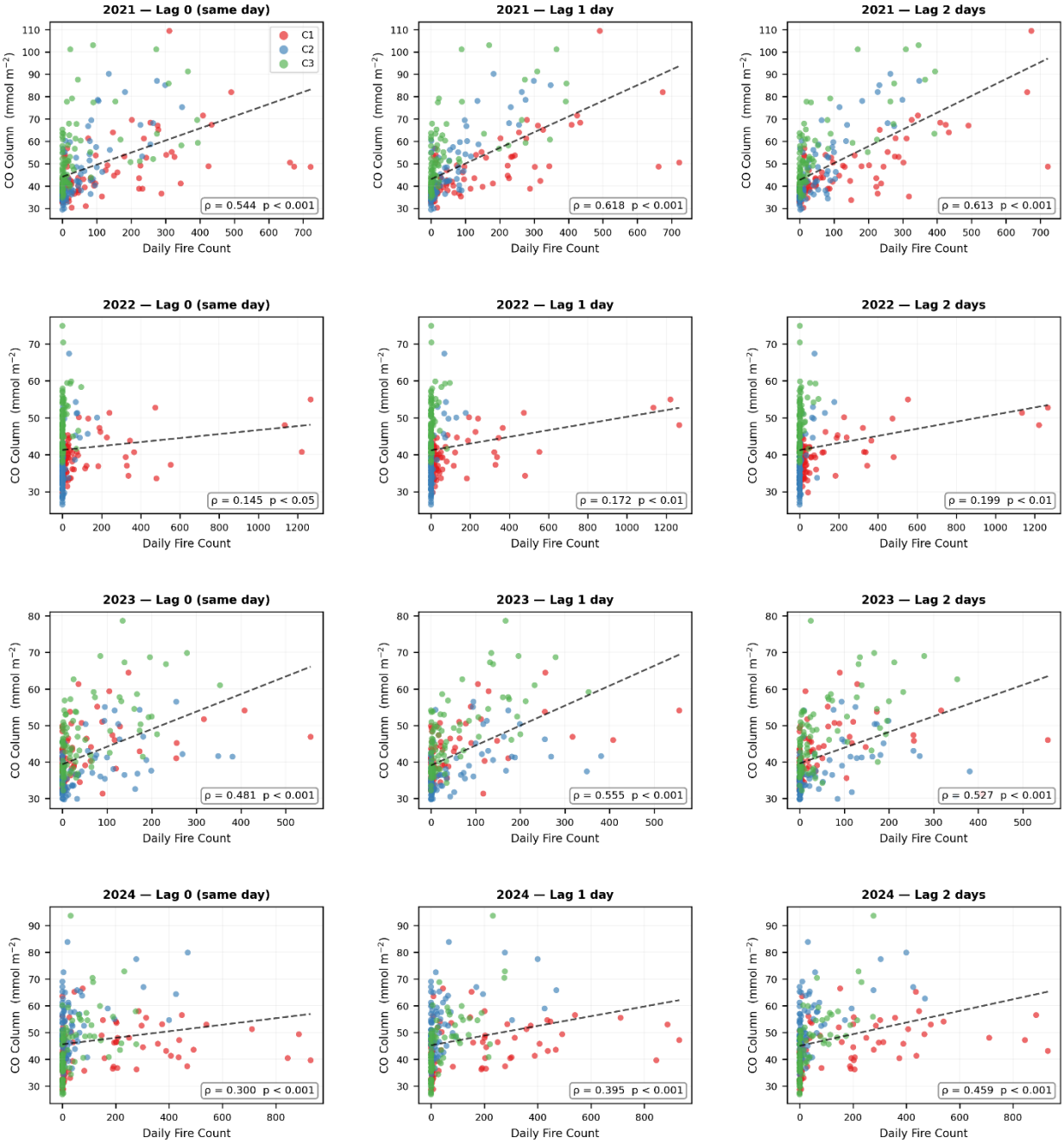

Fig. S5. Spearman correlation between daily fire count and CO column density at lags 0–2 days for each year (2021–2024) and cluster (C1–C3) during March–May.

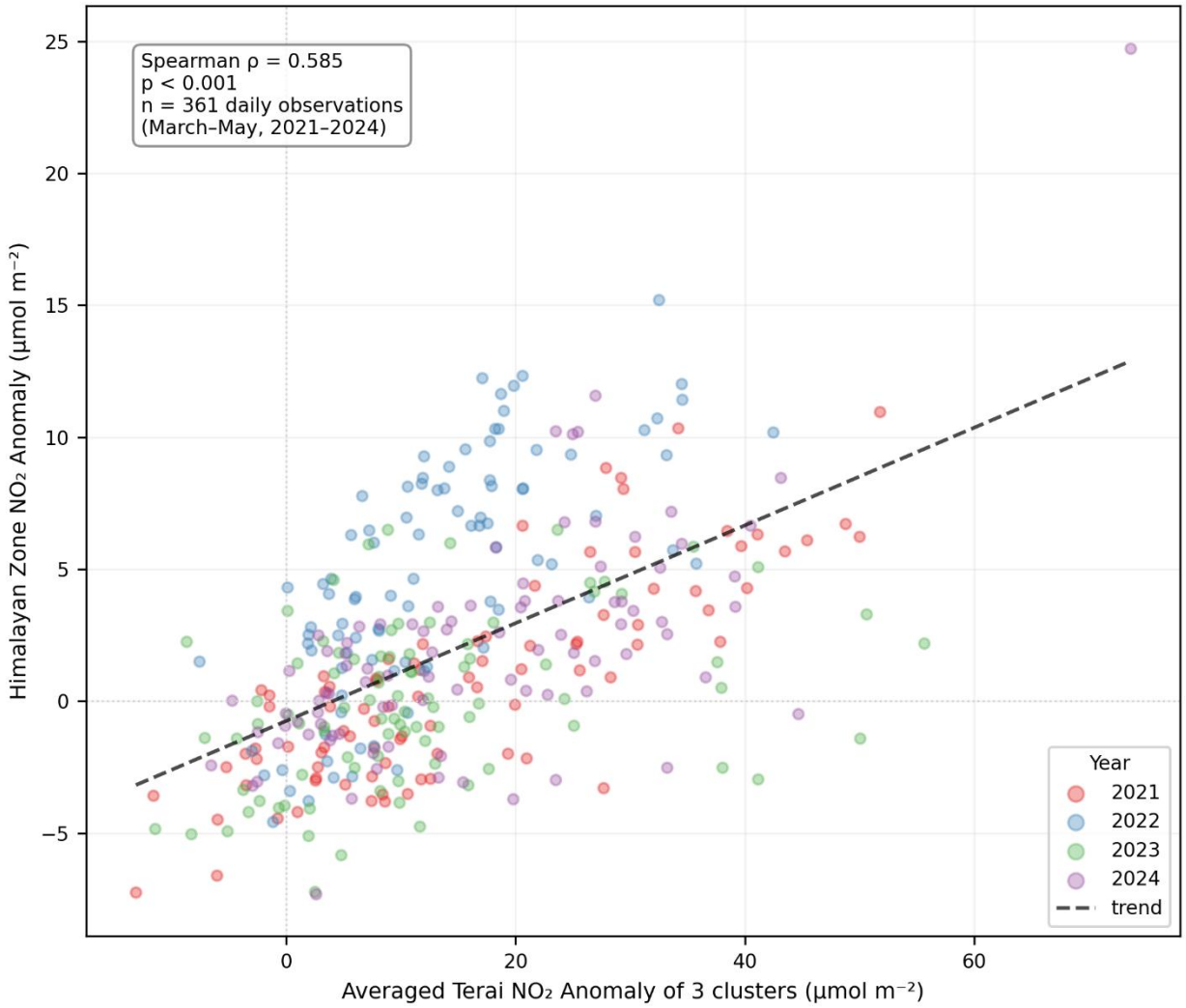

Fig. S6. Same-day Spearman correlation between the averaged NO_2 anomaly across three Terai fire clusters and the Himalayan zone NO_2 anomaly during March–May 2021–2024 .

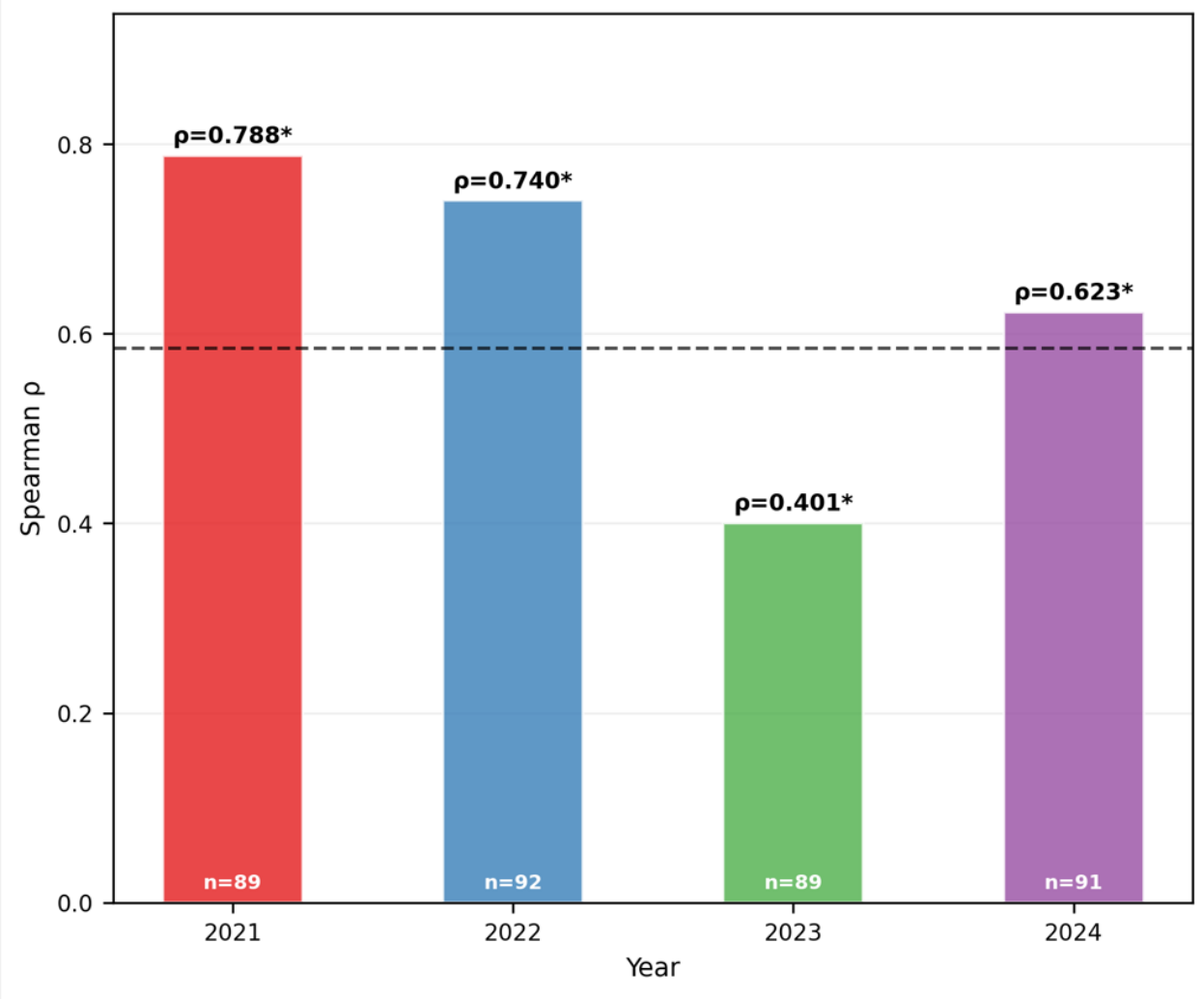

Fig. S7. Year-by-year Spearman correlation between averaged Terai and Himalayan zone NO_2 anomalies during March–May; all years significant ($p < 0.05$). Dashed line indicates the pooled correlation across all four years combined ($\rho = 0.585$).